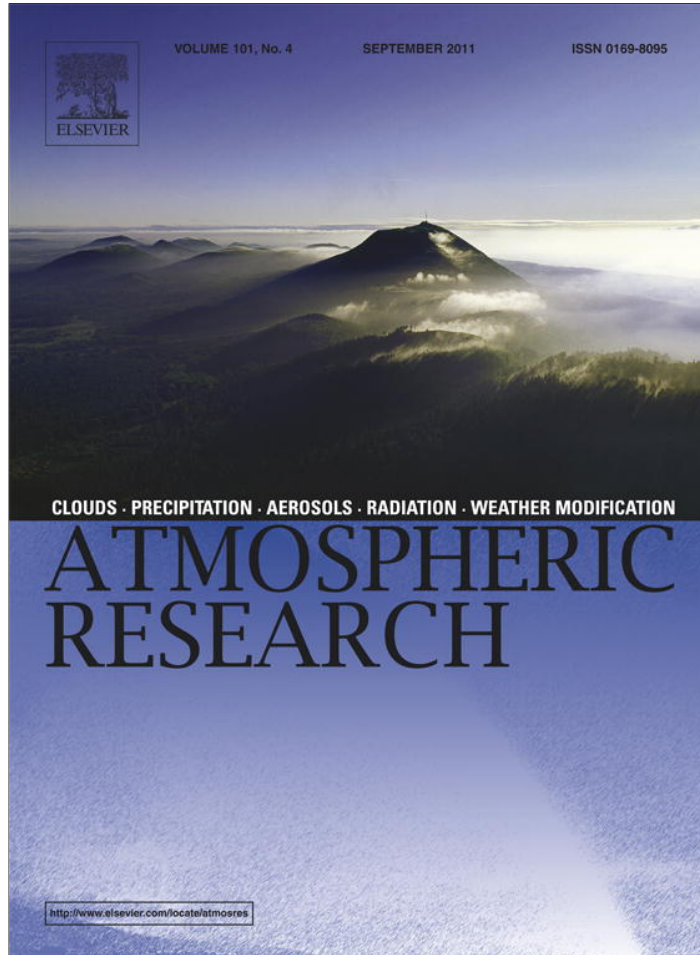


Provided for non-commercial research and education use.
Not for reproduction, distribution or commercial use.



This article appeared in a journal published by Elsevier. The attached copy is furnished to the author for internal non-commercial research and education use, including for instruction at the authors institution and sharing with colleagues.

Other uses, including reproduction and distribution, or selling or licensing copies, or posting to personal, institutional or third party websites are prohibited.

In most cases authors are permitted to post their version of the article (e.g. in Word or Tex form) to their personal website or institutional repository. Authors requiring further information regarding Elsevier's archiving and manuscript policies are encouraged to visit:

<http://www.elsevier.com/copyright>



Contents lists available at ScienceDirect

Atmospheric Research

journal homepage: www.elsevier.com/locate/atmos



Modeling of the cloud and radiation processes observed during SHEBA

Ping Du ^a, Eric Girard ^{a,*}, Allan K. Bertram ^b, Matthew D. Shupe ^c

^a ESCER Centre, Department of Earth and Atmospheric Sciences, University of Quebec at Montreal, P.O. Box 8888, Station Downtown, Montréal, QC, Canada H3C 3P8

^b Chemistry Department, University of British Columbia, 2036 Main Mall, Vancouver, BC, Canada V6T 1Z1

^c Cooperative Institute for Research in Environmental sciences, University of Colorado and NOAA/ESRL/PSD, Boulder, Colorado, USA

ARTICLE INFO

Article history:

Received 27 September 2010

Received in revised form 28 March 2011

Accepted 27 May 2011

Keywords:

Arctic climate

Clouds

Microphysics

Radiation processes

Ice nuclei

Acid coating

ABSTRACT

Six microphysics schemes implemented in the climate version of the Environment Canada's Global Multiscale Environmental (GEM) model are used to simulate the cloud and radiation processes observed during Surface Heat Budget of the Arctic Ocean (SHEBA) field experiment. The simplest microphysics scheme (SUN) has one prognostic variable: the total cloud water content. The second microphysics scheme (MLO) has 12 prognostic variables. The four other microphysics schemes are modified versions of MLO. A new parameterization for heterogeneous ice nucleation based on laboratory experiments is included in these versions of MLO. One is for uncoated ice nuclei (ML-NAC) and another is for sulfuric acid coated ice nuclei (ML-AC). ML-AC and ML-NAC have been developed to distinguish non-polluted and polluted air masses, the latter being common over the Arctic during winter and spring. A sensitivity study, in which the dust concentration is reduced by a factor 5, is also performed to assess the sensitivity of the results to the dust concentration in ML-AC-test and ML-NAC-test.

Results show that SUN, ML-AC and ML-AC-test reproduce quite well the downward longwave radiation and cloud radiative forcing during the cold season. The good results obtained with SUN are due to compensating errors. It overestimates cloud fraction and underestimates cloud liquid water path during winter. ML-AC and ML-AC-test reproduces quite well all these variables and their relationships. MLO, ML-NAC and ML-NAC-test underestimate the cloud liquid water path and cloud fraction during the cold season, which leads to an underestimation of the downward longwave radiation at surface. During summer, all versions of the model underestimate the downward shortwave radiation at surface. ML-AC and ML-NAC overestimate the total cloud water during the warm season, however, they reproduce relatively well the relationships between cloud radiative forcing and cloud microstructure, which is not the case for the most simple scheme SUN.

© 2011 Elsevier B.V. All rights reserved.

1. Introduction

Observations and climate projections (e.g., Johannessen et al., 2004; Arctic Climate Impact Assessment, ACIA, 2004) have shown that the Arctic is a region of particular vulnerability to global climate change. Cloud and radiation processes and their interrelationships with atmospheric dynamics and the underlying boundary layer are complex physical processes that determine the climate projection of the Arctic.

Observations taken during the Surface Heat Budget of the Arctic Ocean (SHEBA) field experiment have shown that cloud fraction ranges from a minimum of about 0.4 during winter and a maximum of 0.8 during summer over the Arctic Ocean. Mixed-phase clouds dominate over ice and liquid clouds despite very cold temperatures characterizing the winter season (Shupe et al., 2006). Boundary layer shallow stratus clouds are frequent during winter and often characterized by a very thin liquid layer below which ice crystals dominate. In summer, multiple thin layers of clouds are common.

Due to the unique conditions in the Arctic (e.g., extreme low temperatures and water vapor, highly reflective sea-ice/snow surfaces, low-level inversions, and the absence of solar radiation

* Corresponding author. Tel.: +1 514 987 3000x3325.
E-mail address: girard.eric@uqam.ca (E. Girard).

for extended periods) clouds have a large influence on the surface radiative energy balance (Wang and Key, 2003). The net effect of clouds on the surface energy budget is especially important over the Arctic Ocean because it can significantly impact sea ice and snow melting, refreezing, thickness and spatial distribution (Maykut and Untersteiner, 1971; Curry and Ebert, 1990). According to Intrieri et al. (2002a), clouds over the Beaufort Sea act to warm the surface for most of the annual cycle with a brief period of cooling in the middle of summer.

To estimate the effect of cloud on the radiation budget, cloud radiative forcing (CRF) was introduced by Ramanathan et al. (1989) as a simple and convenient way to characterize the cloud effect on the net radiation either at the surface or at the top of the atmosphere. CRF is defined as the difference between the net radiative flux in the presence of clouds and the net radiative flux without the presence of clouds. It can also be separated into its longwave and shortwave components. CRF depends on cloud height, thickness, temperature, thermodynamic phase and particle size (Francis, 1999; Curry and Ebert, 1992; Walsh and Chapman, 1998). Using a neural network, Chen et al. (2006) have shown that the surface longwave cloud forcing (CRFL) strongly depends on the cloud liquid water path for optically thin clouds with a saturation effect for thicker clouds. The thermodynamic phase of cloud appears to be an important factor modulating the CRF at surface. Shupe and Intrieri (2004) have shown that the CRFL can reach 40 W m^{-2} when liquid is present as opposed to much smaller values for ice clouds. During SHEBA, CRF was positive most of the year except for a very short period of time in early July (Intrieri et al., 2002a). Even if the North Slope of Alaska is close to the SHEBA site, CRF was considerably different in summer with large negative CRF values due to smaller surface albedo (Shupe and Intrieri, 2004; Dong et al., 2010).

The cloud thermodynamic phase is therefore one of the key variables to reproduce if one wants to properly simulate the CRF. The ice nuclei (IN) concentration plays a critical role in determining the thermodynamic phase and indirectly the CRF through the partitioning of cloud water between liquid and ice. Current models have difficulties simulating the cloud thermodynamic phase in the Arctic (Morrison et al., 2008; Morrison and Pinto, 2006; Morrison et al., 2003; Girard and Curry, 2001). According to Intrieri et al. (2002a), cloud fraction is also a key parameter for CRF. However cloud fraction is still a variable that climate models generally simulate poorly (Randall et al., 1998; Wyser et al., 2008). Although the latest generation of GCMs shows some improvement over older simulations, state-of-the-art models show considerable spread in simulated climatological mean Arctic cloud fractions and its annual cycle (Walsh et al., 2002). According to Wyser et al. (2008), the current regional climate models also have difficulties properly simulating cloud and radiation processes over the Arctic. The Arctic Regional Climate Model Intercomparison Project (ARCMIP) has also revealed that regional climate models have difficulties in properly simulating cloud fractions and the relationships between cloud microphysics and radiation at the surface (Wyser et al., 2008). Inoue et al. (2006) have compared three regional climate models participating in the ARCMIP experiment for the simulation of May 1998. They found that cloud microphysical properties and/or the vertical profile of humidity and temperature were poorly simulated by some models leading to a poor simulation of the radiative budget at surface.

For the whole SHEBA year, Tjernstrom et al. (2008) have compared six models participating to the ARCMIP experiment for the simulation of cloud and radiation processes. They found that models substantially underestimate the liquid water path during the cold season, which leads to an underestimation of the downward longwave radiation at the surface. During summer, cloud base was generally too cold, thus producing a negative longwave radiation bias. Downward solar radiation was also underestimated because models overestimated solar attenuation for a given cloud water path.

To improve cloud-radiation simulations, more work is first needed to better simulate cloud properties. One of the key microphysical processes determining the cloud microstructure is ice crystal nucleation, which essentially depends on aerosol chemical composition. Large concentrations of aerosols are often observed in the Arctic (Schnell, 1984; Yliuomi et al., 2003), especially during winter and spring, which makes the Arctic one of the most polluted regions on Earth during the cold season. These aerosols are mostly coated with sulfuric acid (Bigg, 1980). Laboratory experiments and field observations suggest that acidic coatings on IN can have an important effect on homogeneous and heterogeneous ice nucleation. Archuleta et al. (2005) have shown that the decrease of ice nucleation at temperatures above -40°C by immersion and condensation modes due to a sulfuric acid coating is variable and depends on the IN chemical composition. Other laboratory experiments performed at temperatures ranging between -10 and -40°C also show that the heterogeneous freezing temperature initiated by immersion of various mineral dust particles decreases as the percentage by weight of sulfuric acid in the particle increases (Ettner et al., 2004). More recently, Eastwood et al. (2009) have shown that ice nucleation on kaolinite particles coated with sulfuric acid is considerably altered at temperatures below 243 K, requiring an additional 30% ice supersaturation for ice nucleation to occur when compared to uncoated kaolinite particles. Other laboratory experiments on coated and uncoated mineral dust particles have been performed by Knopf and Koop (2006), Salam et al. (2007) and Möhler et al. (2008) with similar results. Measurements taken during the Arctic Gas and Aerosol Sampling Program (AGASP) in the Arctic have also shown a drastic reduction of the IN concentration when sulfate concentrations are high (Borys, 1989).

The understanding and modeling of cloud and radiation processes will only be possible with a better understanding of the ice nucleation processes and with a better representation of the other cloud microphysical processes affecting cloud microstructure. This research aims to improve the simulation of Arctic cloud characteristics and their effect on the surface energy budget. To reach this objective, a new parameterization of heterogeneous ice nucleation is implemented into the two-moment microphysics scheme of Milbrandt and Yau (2005) to account for the highly polluted environment of the Arctic during winter. The new parameterization is based on laboratory experiments of Eastwood et al. (2008; 2009) cited above for kaolinite particles either uncoated or coated with sulfuric acid. The original version of the Milbrandt and Yau (2005) scheme is also evaluated in addition to a much simpler one-moment microphysics scheme (Sundqvist, 1978). These four microphysics schemes were implemented into the climate version of the Canadian Global Environmental Multiscale Model (GEM). The original and modified versions of these microphysics schemes

are evaluated against cloud and radiation observations taken during the SHEBA field experiment. The importance of heterogeneous ice nucleation for cloud thermodynamic phase and CRF is discussed based on the results.

The paper is organized as follows. Section 2 describes the methodology for this study, which includes the model description, the microphysics schemes used in this study, the simulation configuration and the observation dataset. Then Section 3 follows up with the simulation results from the cloud microphysics schemes and the comparison against the observations. The conclusion and summary will be given in Section 4.

2. Model, observations dataset and design of the experiment

2.1. Global environmental multiscale model

The limited-area version of the Global Environmental Multiscale Model (GEM) is used for this study. The numerical formulation of the model is described in detail in Côté et al. (1998). In this section, the emphasis will be put in the description of the physics package of the model with a particular attention to the microphysics schemes that are used in the simulations as well as the modifications made to these schemes for the treatment of heterogeneous ice nucleation.

The radiation scheme is from Li and Barker (2005) and is based on the correlation-k method with 9 bands in the longwave frequencies and 3 bands in the shortwave frequencies. Emission and absorption of the following gaseous species are accounted for: H₂O, CO₂, O₃, N₂O, CH₄, CFC11, CFC12, CFC13 and CFC14. The land-surface scheme ISBA (Interactions Soil–Biosphere–Atmosphere) developed by Noilhan and Planton (1989) is used to determine the lower boundary conditions for the vertical diffusion of temperature, moisture, and momentum, as well as evaluating the evolution of ten prognostic variables: surface temperature, mean soil temperature, near-surface soil moisture, liquid and frozen bulk soil water contents, liquid water retained on the foliage of the vegetation canopy, equivalent water content of the snow reservoir, liquid water retained in the snow pack, snow albedo, and relative snow density. Turbulent fluxes in the atmosphere and between the atmosphere and the surface are based on a time-dependent prognostic turbulent kinetic energy (TKE) and a mixing length described by Bougault and Lacarrère (1989) and Béclair et al. (1999). The parameterization of the deep and shallow convection is from Kain–Fritsch (Kain and Fritsch 1990, 1993) and the Kuo transient scheme (Kuo 1965, Béclair et al., 2005), respectively.

2.2. Original version of the microphysics schemes

The cloud microphysics schemes used in this study include the Sundqvist scheme (Sundqvist, 1978, hereafter SUN), and the two-moment version of the Milbrandt–Yau scheme (Milbrandt and Yau, 2005).

SUN has one prognostic variable, the total cloud water mixing ratio with a diagnostic partitioning into cloud liquid and ice water based on the local air temperature ranging from all ice at -38°C to all liquid at 0°C (Boudala et al., 2004). Ice crystal heterogeneous nucleation is allowed only if the saturation with respect to liquid water is reached. The autoconversion of cloud water to rain is possible when a fixed threshold value of the

liquid water content is reached. Rain and snow are assumed to precipitate instantaneously. Rain cannot freeze to form snow. Snow melting is possible above the freezing point. SUN also accounts for partial cloudiness, which is based on the relative humidity. Therefore, it is possible to form cloud even if the mean relative humidity of a given model tile is below 100%.

The Milbrandt–Yau scheme used in this study is the two-moment version of this scheme. The prognostic variables are the mixing ratio and the number concentration of six species: cloud liquid water, cloud ice water, rain, snow, graupel, and hail. A gamma size distribution is assumed for the hydrometeors. The scheme allows for the slow sedimentation of ice crystals. Rain and snow do not precipitate instantaneously and can interact with cloud ice and liquid through collision processes. Partial cloudiness is not included in this scheme. The relative humidity with respect to ice or liquid water has to be reached in a tile for the cloud to form. Ice nucleation is permitted as soon as saturation with respect to ice is reached. Deposition and condensation-freezing ice nucleation are based on the empirical relationship of Meyers et al. (1992). Contact ice nucleation is parameterized following Young (1974). The warm microphysical processes are based on Cohard and Pinty (2000). The cold microphysical processes are based on Murakami (1990), Ferrier (1994), Meyers et al. (1997), and Reisner et al. (1998). A detailed description of the treatment of various microphysical processes is available in Milbrandt and Yau (2005). More details are given below for the parameterization of ice nucleation.

2.3. Modified version of the Milbrandt–Yau scheme

During the cold season in the Arctic, most aerosols in the accumulation mode are coated with sulfuric acid (Bigg, 1980). In order to account for the effect of acid coatings on ice nucleation, the parameterization of deposition ice nucleation has been modified in the Milbrandt–Yau scheme. The new parameterization for ice nucleation used in this study is based on the classical theory of heterogeneous ice nucleation of Fletcher (1962). It is assumed that there are no surface active sites for ice nucleation. The only additional unknown parameter is the contact angle (Θ) between the ice embryo and the IN. The contact angle has been derived using the results of the laboratory experiments of Eastwood et al. (2008; 2009) on ice nucleation on uncoated kaolinite particles ($\Theta_{\text{uncoated}} = 12^{\circ}$) and on kaolinite particles coated with sulfuric acid ($\Theta_{\text{coated}} = 27^{\circ}$). The following equation is then used to determine the concentration of ice crystals (N_{ice}) nucleated in a given time step (Δt):

$$N_{\text{ice}}(\Delta t) = \kappa N_{\text{kaolinite}} \quad \text{where} \quad \kappa = [1 - \exp(-JA_{\text{kaolinite}} \Delta t)] \quad (1)$$

where κ represents the fraction of dust particles on which ice nucleation occurs in a given time step, $A_{\text{kaolinite}}$ is the surface area of the kaolinite particles, $N_{\text{kaolinite}}$ is the total concentration of kaolinite particles, and J is the nucleation rate of ice embryo per unit area of the particle and is defined as:

$$J\left(\text{cm}^{-2}\text{s}^{-1}\right) = B \exp\left(\frac{-\Delta G^*}{kT}\right) \quad \text{where} \quad \Delta G^* = \frac{16\pi\sigma_{\text{iv}}^3 f(\cos\Theta)}{3(\rho_i R_v T \ln S_i)^2}$$

where B is the pre-exponential factor, ΔG^* is the critical Gibbs free energy for the formation of an ice embryo, k is the Boltzman

constant, σ_{iv} is the surface tension between ice and water vapor, ρ_i is the bulk ice density, R_v is the gas constant for water vapor, T is the temperature, and S_i is the saturation ratio with respect to ice. $f(\cos \Theta)$ is a function that depends on the contact angle as defined by Pruppacher and Klett (1997) for an infinite plane surface. Since the model is not coupled with an aerosol module, $N_{kaolinite}$ has been prescribed to a fixed value of 0.38 cm^{-3} . This number concentration corresponds to a mass concentration of kaolinite particles of approximately 500 ng m^{-3} and a radius of $0.5 \mu\text{m}$. To assess the sensitivity of this parameter on the results, simulations using a prescribed dust concentration reduced by a factor 5 have also been performed. The dust concentration is highly variable and depends on the large-scale atmospheric circulation. During the AGASP field experiment, dust concentrations were of the order of 100 ng m^{-3} most of the time with few events with concentrations reaching $3 \mu\text{g m}^{-3}$ (Winchester et al., 1984). The prescribed values for $N_{kaolinite}$ are representative of these observations.

Simulations with both the acid-coated scenario and non-coated scenario of the heterogeneous ice nucleation processes are performed with the Milbrandt–Yau scheme.

2.4. Design of the experiment

The experiment described here focuses on the SHEBA year from October 1997 to September 1998. The simulation domain is centered on the Western Arctic covering the SHEBA icebreaker path. Initial and lateral boundary conditions for the atmospheric prognostic variables are obtained from the 6-hourly European Centre for Medium-Range Weather Forecasts (ECMWF) operational re-analyses. Sea ice and sea surface temperature are from the ECMWF 6-hourly reanalysis data.

Simulations are performed with a horizontal resolution of 0.1° and 53 vertical levels with the top at 10 hPa. The time step is 300 s. The period simulated is from March 1997 to September 1998 with the first six months for spinup. This experimental design was approximately the same as the one used for the Arctic Regional Climate Model Intercomparison Project (ARCMIP) (Wyser et al., 2008). This allows for a comparison with results obtained by the regional climate modeling groups who participated to ARCMIP.

Six simulations were performed for this study. Each simulation uses a different microphysics scheme or a different version of the same microphysics scheme. The first simulation was performed using the SUN scheme, while the 5 other simulations use the Milbrandt–Yau scheme: the original Milbrandt–Yau scheme (MLO), the new modified Milbrandt–Yau scheme with the acid-coated kaolinite scenario (ML-AC), and the new modified Milbrandt–Yau scheme with the uncoated kaolinite scenario (ML-NAC). ML-AC and ML-NAC are also evaluated using a dust concentration reduced by a factor 5 (ML-AC-test and ML-NAC-test respectively).

2.5. Observation data set

Model results are compared to the integrated SHEBA dataset, which can be found in <http://www.atmos.washington.edu/~roode/SHEBA.html>. This data set includes meteorological surface observations, surface shortwave downward radiation (SWD), longwave downward radiation (LWD), liquid water path (LWP), water vapor path (WVP), and surface albedo (AL).

The LWD, SWD, and AL were measured from the Atmospheric Surface Flux Group (ASFG) tower (Persson et al., 2002). The LWP values were retrieved from the microwave radiometer (Liljergren, 1999). The measured ice water path (IWP) is obtained from the NOAA Environmental Technology Laboratory (ETL) radar-based cloud microphysics dataset from the SHEBA ice camp, which combined the ground-based radar and radiometer measurements. IWP is calculated using an empirical relationship that relates cloud ice water content to radar reflectivity (Shupe et al., 2001, 2005).

The observed cloud fraction (CF) used for validation is from the AVHRR Polar Pathfinder (APP) (Fowler et al., 2002) dataset. The APP project provides twice per day gridded and calibrated satellite channel data and derived parameters. Cloud fraction is calculated as the fraction of cloudy pixels in an 11 by 11 pixel array centered on the SHEBA site.

The hourly observed surface cloud radiative forcing dataset is from Intrieri et al. (2002a). In this dataset, the clear sky surface radiation fluxes were calculated by the Santa Barbara Discrete Ordinate Radiative Transfer (DISORT) Atmospheric Radiative Transfer model (SBDART) with the inputs of the rawinsonde sounding information. The cloudy radiation fluxes at the surface are from the measurements. More details on observations are available in Intrieri et al. (2002a).

3. Results

In this section, monthly and daily averaged radiation fluxes are compared to the SHEBA observations. Important variables affecting cloud radiative forcing are also evaluated such as cloud fraction, LWP, IWP, and surface albedo. Linear interpolation between grid boxes is used to find the simulated value of a given variable at the SHEBA site, which is often located relatively far from the center of a grid box.

3.1. Monthly-averaged analysis

Fig. 1 shows the monthly-averaged liquid water path (LWP) and ice water path (IWP) for the SHEBA year. The observed LWP is minimum in winter and maximum during the warm season. This is consistent with the highest values of specific humidity occurring during the warm season. The IWP however does not have a clear annual cycle; it remains more or less constant over time. The six versions of the model reproduce quite well the LWP and IWP annual cycle. However they differ substantially from each other for IWP and LWP absolute values. SUN generally underestimates the LWP and overestimates the IWP except during winter where both LWP and IWP are underestimated. Similar results with SUN were obtained with the same model by Dorais et al. (2008) for the simulation of clouds observed during the Mixed-Phase Arctic Cloud Experiment (M-PACE) and by Paquin-Ricard et al. (2010) for the simulation of clouds observed at the Atmospheric Radiation Measurements (ARM) Southern Great Plains and North Slope of Alaska sites. The negative bias for LWP and positive bias for IWP obtained in all these studies may be explained by the partitioning of liquid and ice water as a function of temperature which does not reflect the complexity of the physical processes determining cloud phase partition. Paquin-Ricard et al. (2010) have suggested that a too-low threshold of liquid water content for autoconversion might hinder the existence of high-LWP non-precipitating clouds. This

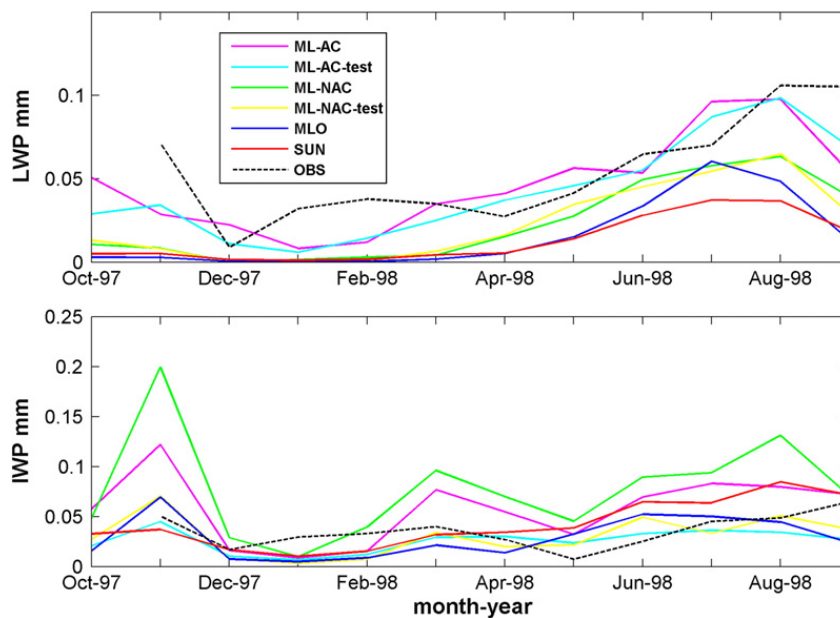


Fig. 1. Observed and simulated monthly mean LWP (mm) and IWP (mm). OBS denotes observations from (i) the microwave radiometer at the SHEBA site (LWP), and (ii) NOAA ETL radar dataset (IWP).

does not appear to be the case in our simulation since precipitation and LWP biases are well correlated.

There are substantial differences between results obtained with the original and modified versions of the Milbrandt–Yau scheme (ML-AC, ML-NAC, ML-AC-test, ML-NAC-test and MLO). ML-AC and ML-AC-test results are the closest to the observed IWP and LWP when compared to the three other versions of Milbrandt–Yau scheme and SUN. The LWP underestimation of ML-AC and ML-AC-test is smaller than the other scheme underestimation for January and February, the coldest months of the year. ML-NAC, ML-NAC-test and MLO generally underestimate the LWP in winter and spring. During summer, ML-NAC-test, ML-AC-test and MLO reproduce reasonably well the IWP while ML-AC, ML-NAC and SUN overestimate the IWP.

Table 1 shows the annual and seasonal averages of LWP and IWP simulated by the six schemes and observed for the period November 1997 to September 1998. It should be noted that the uncertainty in the observations are large with $\pm 25 \text{ g m}^{-2}$ for LWP and a factor of ± 2 for the IWP (Shupe et al., 2005). These uncertainties, which are valid for individual IWP and LWP retrieval, are likely smaller for an annual cycle due to the long-term statistical nature of the data set. Table 1 shows that SUN, MLO, ML-NAC and ML-NAC-test fall below the range of possible values from the observations for LWP annual average and within the observed range for IWP (except for ML-NAC). LWP simulated by ML-NAC and ML-NAC-test is however closer to the observed uncertainty range for LWP compared to MLO and SUN. The only schemes with both simulated yearly averaged IWP and LWP within the observation range are ML-AC and ML-AC-test. During winter, SUN, MLO, ML-NAC and ML-NAC-test strongly underestimate the LWP while ML-AC and ML-AC-test are within the observed LWP uncertainty observation range. In spring and summer, the former schemes still underestimate the LWP but to lesser extent. The simulated yearly averaged IWP is well captured by all schemes, except for ML-NAC. The slight yearly averaged IWP overestimation of this scheme is due to the substantial overestimation of IWP during summer. The total

cloud water path differs quite substantially between the schemes. SUN, MLO and ML-NAC-test simulate the lowest values (yearly averaged) while ML-AC and ML-NAC simulate a total cloud water path twice as large when compared to SUN and MLO. The low total water path simulated by SUN, MLO and ML-NAC-test is due to the substantial underestimation of the total water path during winter. The total cloud water path simulated by ML-AC-test is between these two groups.

The relatively low values of the total cloud water path by SUN is related to the amount of condensed water the scheme can produce when the atmosphere is saturated with respect to ice but subsaturated with respect to liquid water. Indeed, for SUN, it is not possible to nucleate ice crystals before saturation with respect to liquid water is reached. Therefore, at low temperatures, the atmosphere can remain for a long period of time between the two saturation points (liquid and ice) and no cloud formation is possible with this scheme. MLO, ML-NAC and ML-NAC-test behave similarly to each other. In these schemes, heterogeneous nucleation is possible when the air is saturated with respect to ice and sub-saturated with respect to water. In such an environment, the available water vapor deposits on the nucleated ice crystals and can maintain the atmosphere sub-saturated with respect to liquid water in cases where the air mass cooling rate is relatively small. This is why the simulated LWP is relatively small in these schemes. The IWP difference between the three schemes reflects the availability of ice nuclei in sub-saturated environment with respect to liquid water. Differences of simulated LWP and IWP between ML-NAC and ML-AC are directly related to the lower nucleation rate of ice crystals occurring in sub-saturated air with respect to liquid water in ML-AC. Saturation with respect to liquid water is more often reached in ML-AC and this allows for a higher LWP and lower IWP when compared to ML-NAC. Differences between ML-AC and ML-AC-test and between ML-NAC and ML-NAC-test show the sensitivity of the results to the dust concentration. In the low dust concentration scenarios (AC-test and NAC-test), the concentration of activated ice nuclei is much smaller resulting in

Table 1

LWP, IWP, total cloud water and the ratio of liquid total cloud water of ML-AC, ML-AC-test, ML-NAC, ML-NAC-test, MLO, SUN and from observations (OBS) respectively. Annual, DJF, MAM and JJA averages are shown. The uncertainty range is provided for OBS.

	LWP (g/m ²)	IWP (g/m ²)	Total cloud water (g/m ²)	LWP/TCW
<i>Annual average</i>				
ML-AC	45.9	57.3	103.2	0.45
ML-AC-test	43.9	26.1	70.0	0.63
ML-NAC	24.6	79.4	104.0	0.24
ML-NAC-test	23.7	30.5	54.2	0.44
MLO	16.5	29.9	46.4	0.36
SUN	14.0	42.6	56.6	0.25
OBS	54.5	35.2	89.7	0.61
	(29.9–79.5)	(17.6–70.4)	(47.5–149.9)	
<i>DJF</i>				
ML-AC	14.1	13.5	27.6	0.51
ML-AC-test	10.4	9.7	20.1	0.52
ML-NAC	1.6	26.0	27.6	0.06
ML-NAC-test	0.7	6.2	6.9	0.11
MLO	0.3	7.0	7.3	0.04
SUN	1.4	14.2	15.6	0.09
OBS	32.0	26.5	58.5	0.55
	(7.0–57.0)	(13.3–52.0)	(20.3–109.0)	
<i>MAM</i>				
ML-AC	44.2	54.4	98.6	0.45
ML-AC-test	36.0	27.7	63.7	0.57
ML-NAC	15.7	70.5	86.2	0.18
ML-NAC-test	19.1	25.2	44.3	0.43
MLO	7.4	22.5	29.9	0.25
SUN	7.9	34.9	42.8	0.18
OBS	40.7	24.7	65.4	0.62
	(15.7–65.7)	(12.4–49.4)	(28.1–115.1)	
<i>JJA</i>				
ML-AC	83.0	77.5	160.5	0.52
ML-AC-test	80.2	34.5	114.7	0.70
ML-NAC	56.9	104.8	161.7	0.35
ML-NAC-test	54.9	44.4	99.3	0.55
MLO	47.5	48.9	96.4	0.49
SUN	34.0	71.0	105.0	0.32
OBS	80.2	39.6	119.8	0.70
	(55.2–105.2)	(19.8–79.2)	(75.0–184.4)	

a lower IWP when compared to the high dust concentration scenarios (AC and NAC). The difference between the annual mean IWPs in the acid coated scenarios (AC and AC-test) is not as large as in the uncoated scenarios (NAC and NAC-test). This is explained by the fact that the fraction of dust particles on which ice nucleation occurs (κ in Eq. (1)) at a given temperature and ice supersaturation depends on the contact angle, which is larger in the coated scenarios. Therefore, κ is smaller in the coated scenarios. Thus an increase in the dust concentration (N_{dust} in Eq. (1)) has a smaller impact on the number concentration of ice crystals nucleated. LWP differences between the high versus low dust concentration scenarios are negligible for both the coated and uncoated scenarios (AC and NAC).

Fig. 2 shows the monthly-averaged ratio of cloud liquid water to the cloud total water (liquid and ice) (LWP ratio). Observations show that the LWP ratio varies between 0.4 and 0.6 during winter and increases slightly during spring and summer to values varying between 0.6 and 0.8. SUN, MLO, ML-NAC and ML-NAC-test substantially underestimate the LWP

ratio for the whole period. ML-AC reproduces the winter values but does not capture the increase of the LWP ratio during summer. This is related to the overestimation of the IWP of ML-AC during summer. ML-AC-test is the best version of the model with LWP ratio values close to the observations in all seasons (see Table 1).

The monthly averaged shortwave downward radiation (SWD) and longwave downward radiation (LWD) at the surface are shown in Fig. 3. LWD and SWD strongly depend on temperature and humidity in addition to cloud, aerosols, and atmospheric gasses. The mean vertical profile of temperature and humidity for both winter and summer are relatively well simulated (not shown). The simulated temperature for both winter and summer remains within 1 °C of the observed temperature for all versions of the model. During winter, all versions are a bit too moist in the lowest 500 m, which indicates an overestimation of the specific humidity of up to 16%. SUN is too dry between 900 and 750 hPa with an underestimation of the specific humidity of 5%. During summer, all versions of the model are close to the observations with relative humidity differences of less than 5%.

The observed SWD has a clearly defined annual cycle with a minimum in winter and a maximum during summer. All versions of GEM reproduce this annual cycle with some small differences in timing of the maximum reached and the maximum absolute SWD value. SUN, MLO, ML-NAC, ML-NAC-test and ML-AC-test simulate the maximum a little too early in May instead of June due to a substantial underestimation of cloud fraction in spring (see Fig. 5) while ML-AC captures this SWD maximum at the observed month in June. However, the maximum of SWD simulated by ML-AC is too low and remains too low for the whole summer. ML-NAC, ML-NAC-test and ML-AC-test behave similarly to ML-AC while MLO and SUN are closer to the observed values. Table 2 shows that the annual averaged bias (simulated values – observed values) of SWD are -9.02 , -6.25 , -6.79 , -0.31 , 5.09 , and 0.67 W m^{-2} for ML-AC, ML-AC-test, ML-NAC, ML-NAC-test, MLO and SUN, respectively. The underestimation of SWD by ML-AC and ML-NAC is partly related to the overestimation of the total cloud water of these schemes. Clouds are optically thicker, thus contributing to increase cloud albedo. Although ML-AC-test does a good job at reproducing the LWP and IWP during summer, it underestimates the SWD. This can be due to the overestimation of the CRREL surface albedo, which will be further discussed later. The small bias of ML-NAC-test is the result of an overestimation of SWD in May, July and August and an underestimation of the SWD peak in June.

With regard to LWD, SUN, ML-AC, ML-AC-test and ML-NAC reproduce very well the LWD annual cycle with values close to the observations. ML-NAC-test and MLO have a systematic negative LWD bias for the whole year. This is consistent with the underestimation of these versions of cloud fraction (see Fig. 5) and LWP. An additional contributing factor to this negative LWD bias could be related to cloud height, which has not been examined in this investigation. The annual averaged biases are -0.91 W m^{-2} , -3.56 W m^{-2} , -6.39 W m^{-2} , -12.37 W m^{-2} , -16.70 W m^{-2} , and -0.85 W m^{-2} for ML-AC, ML-AC-test, ML-NAC, ML-NAC-test, MLO and SUN, respectively (see Table 2).

The annual cycle of the simulated and observed surface albedo (AL) is shown in Fig. 4. Two datasets are available for the

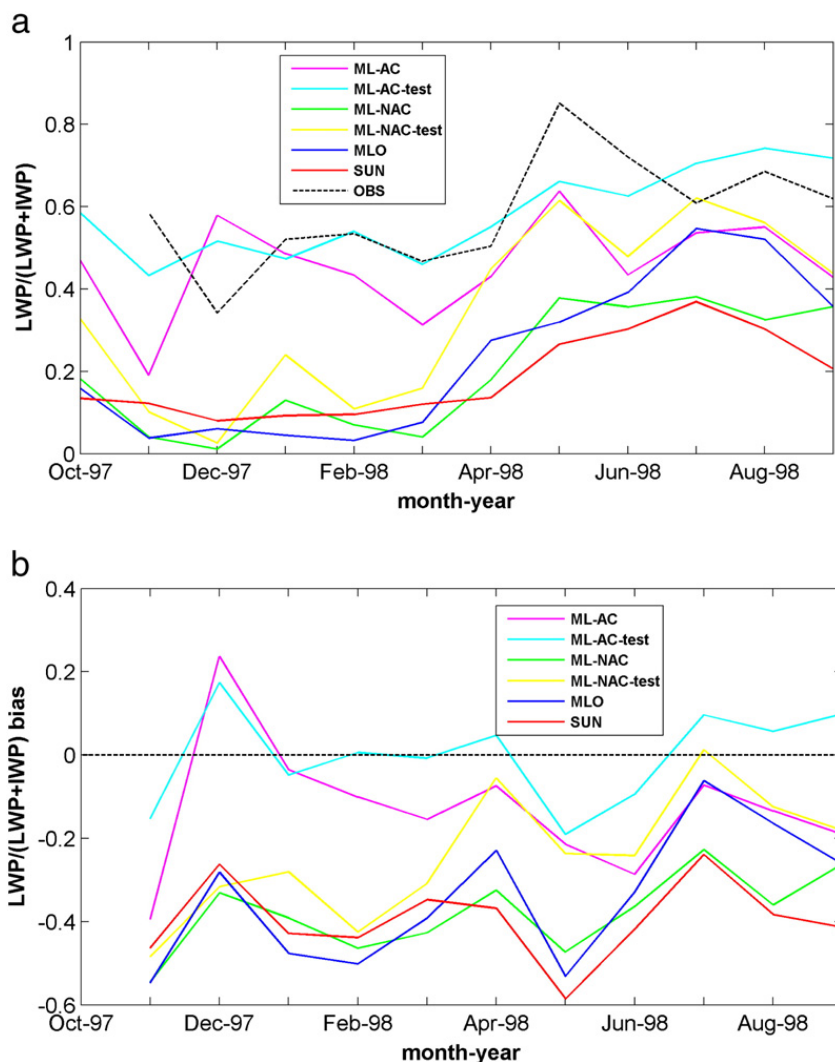


Fig. 2. (a) Observed and simulated monthly mean LWP ratio, namely LWP/(LWP + IWP) and (b) differences between the simulated and observed LWP ratios. OBS from Fig. 1.

surface albedo (Intrieri et al., 2002a). The first one was measured at one single location each hour using a radiometer located at the base of the ASFG tower (see Section 2.5). The second albedo (CRREL albedo, Perovich et al., 2002) was measured once daily along a 200 m line that incorporated different ice types including melt ponds and open water. In winter and early spring, all schemes reproduce the observed ASFG AL but overestimate the CRREL albedo. From May to September, the simulated AL is between the ASFG and CRREL albedos. Differences between modeled AL and observations vary between 0.1 and 0.2. One may argue that because it covers a larger area, the CRREL albedo is probably more representative of a model tile than the ASFG albedo, which represents a single point. This would mean that the simulated AL is too high. Snow albedo depends on snow aging among other things. In our simulations, precipitation measured by a nipher shielded snow

gage system is overestimated during summer (figure not shown). A surplus of fresh snow onto the surface during summer could explain the overestimation of AL. Differences between SUN, MLO, ML-NAC, ML-NAC-test, ML-AC and ML-AC-test for precipitation reflect their differences in the simulated AL. In a coupled model, the AL overestimation could have a large effect on the snow and ice-albedo feedback and sea ice melting.

The monthly mean cloud fraction is shown in Fig. 5. Both satellite and ground-based observations are shown. The latter dataset comes from the Environmental Technology Laboratory (ETL) lidar/radar measurements (Intrieri et al., 2002b; Shupe et al., 2011). Satellite and ETL measurements exhibits the same annual cycle but the ETL cloud fraction is systematically larger by about 10 to 15% when compared to the satellite cloud fraction. Wintertime clouds in the Arctic are often optically thin and are not easily detected by satellites (Curry et al., 1996). This explains

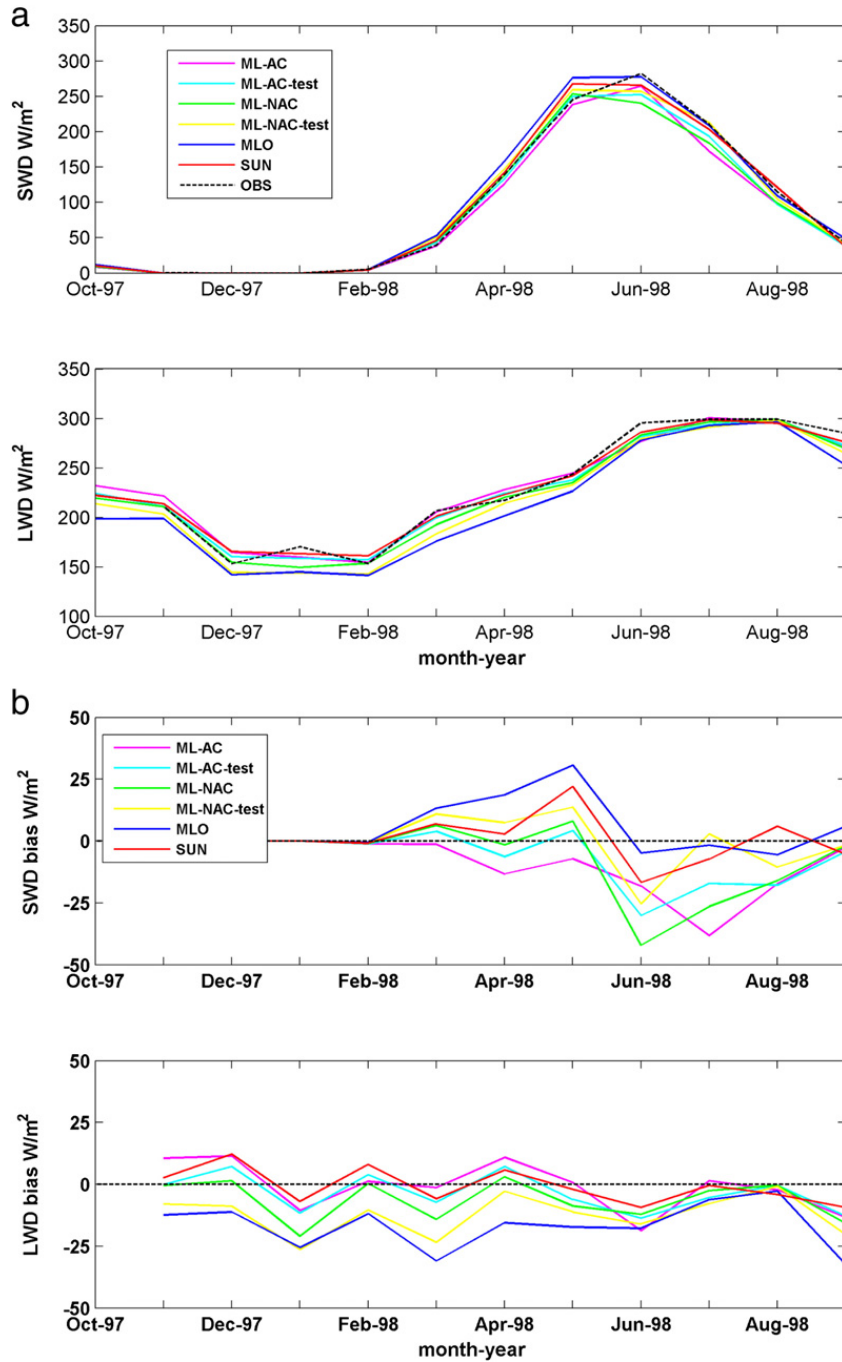


Fig. 3. (a) Observed and simulated monthly mean surface SWD (W/m^2) and LWD (W/m^2) radiation and (b) differences between the simulated and observed monthly mean surface SWD and LWD radiation. OBS denotes observations from radiometers at the SHEBA site.

in part the discrepancy between both instruments. However, one has to keep in mind that the satellite measures cloud cover on a 5 km by 5 km tile while the ETL measures the cloud fraction directly above the instrument. Therefore, even if the satellite measurements were perfect, measurements would likely be different. Therefore, differences between measurements from these two instruments should be viewed as a measure of the uncertainty.

Observations show that the monthly mean cloud fraction is at a minimum during winter with values ranging between 0.5 and 0.6 and it reaches a maximum of nearly 1 during summer.

Compared to the observations, all schemes reproduce quite well the cloud fraction in summer while they generally underestimate it during the winter and spring (see Table 2). SUN substantially overestimates the cloud fraction during the winter and early spring. The five Milbrandt-Yau schemes underestimate the cloud fraction during fall and spring. In winter there is a larger discrepancy between the five schemes. MLO, ML-NAC-test and ML-NAC strongly underestimate the cloud fraction by up to 33% while ML-AC and ML-AC-test are more in agreement with observations with a relatively small underestimation of 4 and 2% respectively (see Table 2). As

Table 2

CF, LWD, SWD, CFLW, CFSW and SCF for ML-AC, ML-AC-test, ML-NAC, ML-NAC-test, MLO, SUN and from observations (OBS) respectively. Annual, DJF, MAM and JJA averages are shown.

	CF	LWD (wm^{-2})	SWD (wm^{-2})	CFLW (wm^{-2})	CFSW (wm^{-2})	SCF (wm^{-2})
<i>Total</i>						
ML-AC	0.67	229.57	89.19	41.59	−22.39	19.20
ML-AC-test	0.64	226.91	91.96	38.80	−22.72	16.08
ML-NAC	0.59	224.09	91.42	36.38	−21.96	14.42
ML-NAC-test	0.49	218.10	97.90	30.96	−20.56	10.40
MLO	0.48	213.77	103.31	28.43	−17.83	10.60
SUN	0.88	229.62	98.88	43.61	−19.33	24.29
OBS	0.73	230.47	98.21	38.18	−10.91	27.27
<i>For DJF</i>						
ML-AC	0.44	159.65	1.40	21.51	−0.08	21.42
ML-AC-test	0.46	158.76	1.39	19.97	−0.08	19.89
ML-NAC	0.27	152.57	1.44	13.54	−0.08	13.46
ML-NAC-test	0.17	143.75	1.59	5.97	−0.05	5.92
MLO	0.15	142.79	1.61	6.40	−0.04	6.36
SUN	0.90	163.41	1.47	26.24	−0.07	26.17
OBS	0.48	158.96	1.78	17.97	0.05	18.02
<i>For MAM</i>						
ML-AC	0.64	226.08	134.41	41.58	−11.04	30.54
ML-AC-test	0.58	220.63	142.30	36.87	−9.61	27.26
ML-NAC	0.55	216.05	145.94	33.03	−8.72	24.31
ML-NAC-test	0.45	210.16	152.36	28.24	−7.79	20.45
MLO	0.39	201.41	162.57	21.46	−5.35	16.11
SUN	0.83	221.98	152.26	40.88	−7.43	33.45
OBS	0.78	222.65	141.66	39.99	−4.29	35.70
<i>For JJA</i>						
ML-AC	0.84	291.49	178.02	53.42	−67.29	−13.87
ML-AC-test	0.83	291.48	180.87	52.55	−68.54	−15.99
ML-NAC	0.88	292.99	174.36	54.29	−67.92	−13.63
ML-NAC-test	0.80	289.77	191.56	50.72	−62.88	−12.16
MLO	0.82	289.09	198.57	52.04	−56.77	−4.73
SUN	0.88	293.34	196.54	56.13	−58.03	−1.90
OBS	0.94	298.01	202.56	48.42	−34.89	13.54

mentioned earlier, the cloud fraction underestimation by MLO and ML-NAC-test explains their underestimation of LWD. However, the cloud fraction overestimation by SUN during winter does not produce any overestimation of LWD as one should expect. Although cloud fraction is too large, the cloud total water path is strongly underestimated in SUN. There are

thus compensating errors that result in a simulated LWD close to the observations during winter.

Fig. 6 shows the comparison of the annual cycle of the cloud radiative forcing at the surface for the net shortwave radiation (CFSW), the net longwave radiation (CFLW), and the total cloud forcing (SCF). The simulated and observed CFSW, CFLW, and

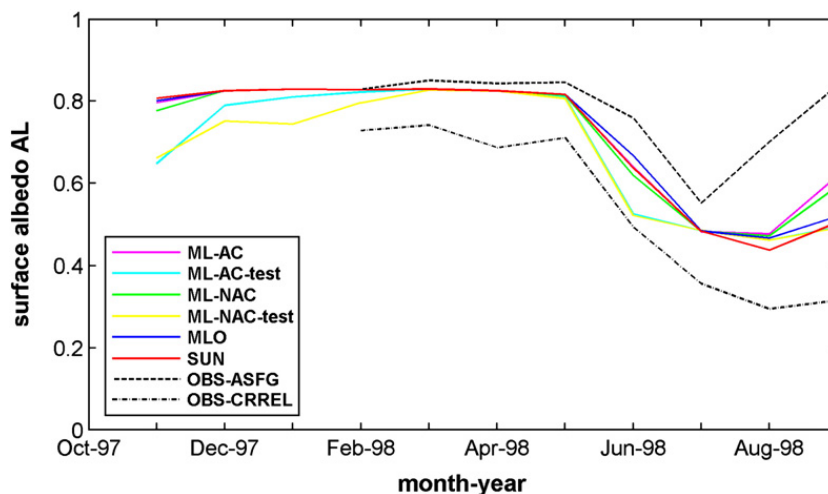


Fig. 4. Observed and simulated monthly mean surface albedo AL. The CRREL and ASFG observed albedos are shown.

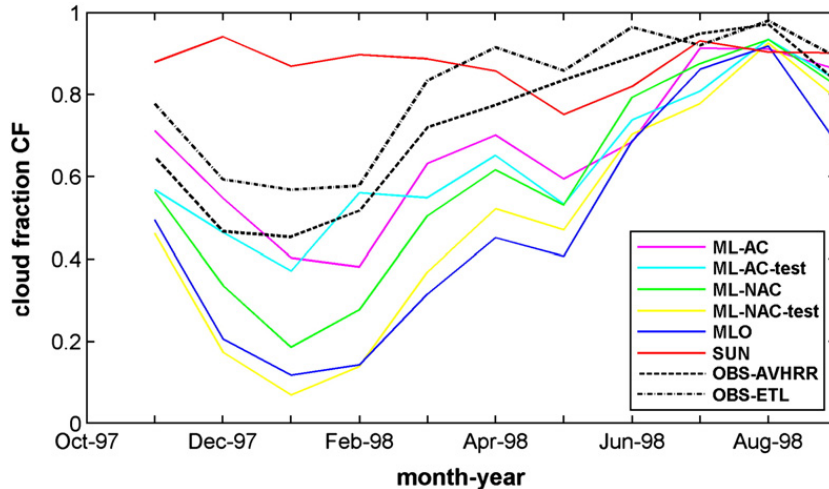


Fig. 5. Observed and simulated monthly mean cloud fraction CF. OBS-AVHRR the AVHRR APP satellite cloud fraction and OBS-ETL is the ETL ground-based lidar/radar measurements.

SCF are averaged over consecutive periods of 20 days to fit the observed cloud forcing dataset of Intrieri et al. (2002a).

The observed CFLW is positive the entire year with values ranging from 15 to 60 W m^{-2} . In winter, clouds are optically thinner as compared to summer. Therefore, their effect on the surface LWD is smaller. Cloud thermodynamic phase is however very important in the magnitude of CFLW. Shupe and Intrieri (2004) have shown that the presence of liquid water in clouds substantially increased the CFLW during SHEBA. During summer, clouds are optically thicker with larger liquid water contents when compared to the cold season. Their infrared emissivity is therefore close to 1. Simulation results show that the model generally reproduces quite well the summertime CFLW values, which vary between 35 and 60 W m^{-2} . All schemes behave similarly during summer with a slight overestimation varying between 2 and 8 W m^{-2} (see Table 2). During winter and spring, results differ substantially depending on the scheme used. MLO and ML-NAC-test are the worst schemes with a substantial underestimation of the CFLW of up to 20 W m^{-2} . This is consistent with the cloud fraction and LWP underestimation of MLO and ML-NAC-test during winter and spring. ML-AC, ML-AC-test, ML-NAC and SUN are the versions of the model being the closest to the observed CFLW as shown by the annual-mean CFLW values of 41 W m^{-2} , 28 W m^{-2} , 41 W m^{-2} , 39 W m^{-2} , 36 W m^{-2} and 31 W m^{-2} for SUN, MLO, ML-AC, ML-AC-test, ML-NAC and ML-NAC-test respectively, compared to the observed CFLW annual mean of 38 W m^{-2} (Intrieri et al. 2002a). Compensating errors allows SUN to be close to the observed CFLW. Indeed, the LWP underestimation (which contributes to decrease the CFLW) is compensated by the overestimation of cloud fraction (which contributes to increase the CFLW). Such compensating errors are not found for ML-AC, ML-AC-test and ML-NAC. These versions of the model better simulate the factors contributing to the CFLW.

Fig. 6b shows the annual cycle of the 20-day mean CFSW. In the Arctic, the CFSW is zero during the cold season due to no insolation. Observations show that the CFSW is at a maximum during summer with negative values reaching -50 W m^{-2}

with an annual mean value close to -11 W m^{-2} . The observed CFSW is calculated using the ASFG radiation and albedo measurements. According to Intrieri et al. (2002b) the ASFG albedo is temporally more representative and consistent than the CRREL albedo. All schemes overestimate the magnitude of CFSW. The annual averaged values of CFSW are -19 W m^{-2} , -18 W m^{-2} , -22 W m^{-2} , -23 W m^{-2} , -22 W m^{-2} and -21 W m^{-2} for SUN, MLO, ML-AC, ML-AC-test, ML-NAC and ML-NAC-test respectively (see Table 2). Contributing factors to the CFSW include cloud fraction, LWP and IWP. Except for ML-AC and ML-AC-test, all schemes underestimate the LWP. Cloud fraction is generally well captured during the warm season by all schemes and the IWP is overestimated by some schemes (ML-AC, ML-NAC and SUN). These LWP biases contribute negatively to the simulated CFSW while the IWP positive biases contribute positively to the CFSW. However, these biases cannot explain entirely the large positive CFSW bias of all schemes. In addition to the clouds themselves, the CFSW also depends on the surface albedo. As shown previously, all schemes underestimate the ASFG surface albedo during spring and summer. The negative bias in the simulated surface albedo clearly plays an important role to the large CFSW bias. ML-AC and ML-NAC are the schemes producing the largest negative bias in surface albedo, which cause the largest overestimation of CFSW when compared to the other schemes. The total simulated SCF reflects the results obtained for CFLW during the cold season and for CFSW for the warm season since the CFLW is quite well simulated by each scheme during the warm season.

3.2. Co-variability of daily average values

The performance of four versions of the model (SUN, MLO, ML-AC and ML-NAC) will be evaluated for their ability to reproduce the co-variability of the CFLW and CFSW with the liquid water path, ice water path, and cloud fraction. Results of the co-variability of daily average values obtained with ML-AC-test and ML-NAC-test are not presented since they are very similar to those obtained with ML-AC and ML-NAC respectively. For this comparison we exploit the daily-mean values from simulations and observations.

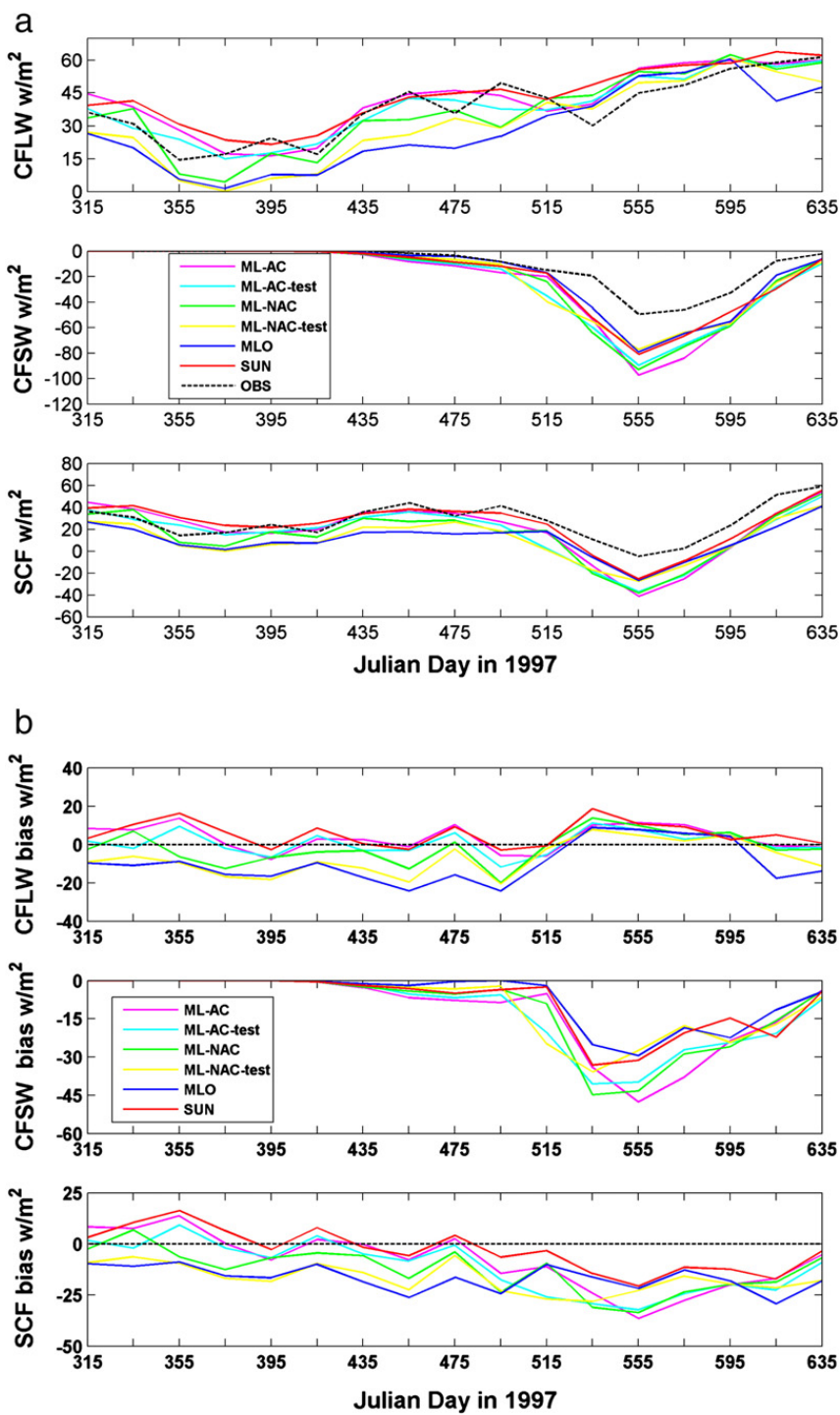


Fig. 6. (a) 20-day averaged observed and simulated CFLW (W/m^2), CFSW (W/m^2) and SCF (W/m^2) and (b) differences between the simulated and observed CFLW, CFSW and SCF. OBS is from the dataset in [Intrieri et al. \(2002a\)](#).

3.2.1. Cloud fraction and SCF

Fig. 7a shows the observed and simulated relationships of CFLW with cloud fraction. Observations show that the maximum of CFLW increases almost linearly with cloud fraction. Scatter in CFLW values increases with cloud fraction due to the variability in cloud microphysical properties and temperature. The four versions of the model reproduce relatively well the gradual increase of CFLW with cloud fraction. The cloud fraction positive bias of SUN is illustrated by the low

density of points for small values of cloud fraction. Nevertheless, SUN captures well the CFLW maximum values for partly cloudy sky ($\text{CF}<0.5$). For cloudier sky ($\text{CF}>0.5$), SUN reproduces well the observed CFLW scatter. The three other versions produce less scatter than SUN for cloudier sky and miss the range of CFLW for overcast skies.

Fig. 7b shows the observed and simulated relationships of CFSW with cloud fraction. Observations show that the CFSW remains relatively small for cloud fraction below 0.5 and

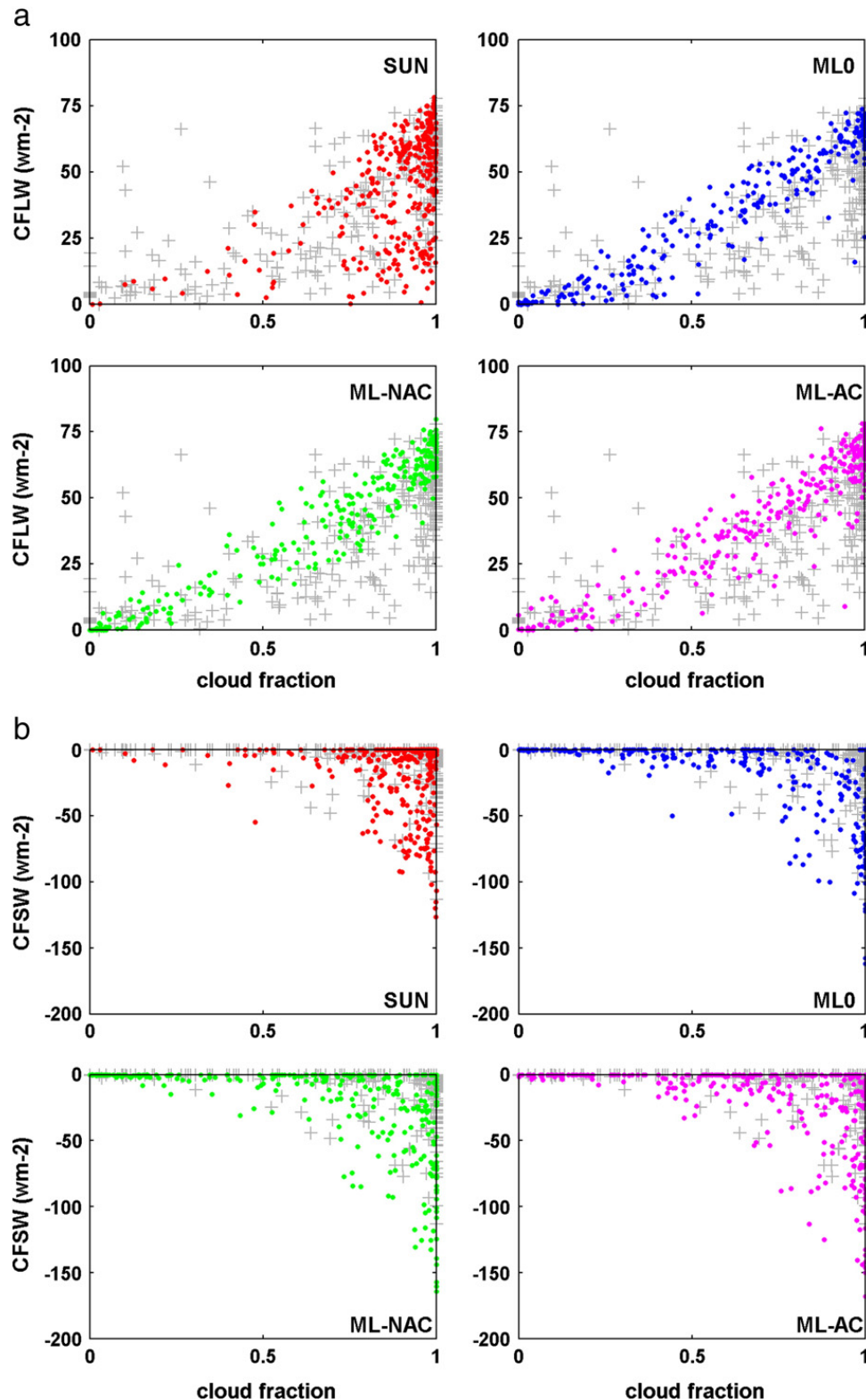


Fig. 7. Simulated and observed (gray crosses) variation of (a) CFLW (W/m^2) and (b) CFSW (W/m^2) with cloud fraction CF.

increases rapidly from 0.5 to 1.0. The four versions of the model qualitatively reproduce quite well this relationship. The simulated CFSW is however overestimated by all schemes when cloud fraction is above 0.5. This overestimation is related to the negative summertime surface albedo bias discussed in the previous section.

3.2.2. Cloud water and SCF

Fig. 8a shows the observed and simulated relationship of CFLW with LWP. The observed CFLW increases rapidly with LWP between 0 and 30 g m^{-2} . Above this value, LWP increase has no further impact on the CFLW. This is known as the longwave saturation effect. CFLW scatter for low LWP

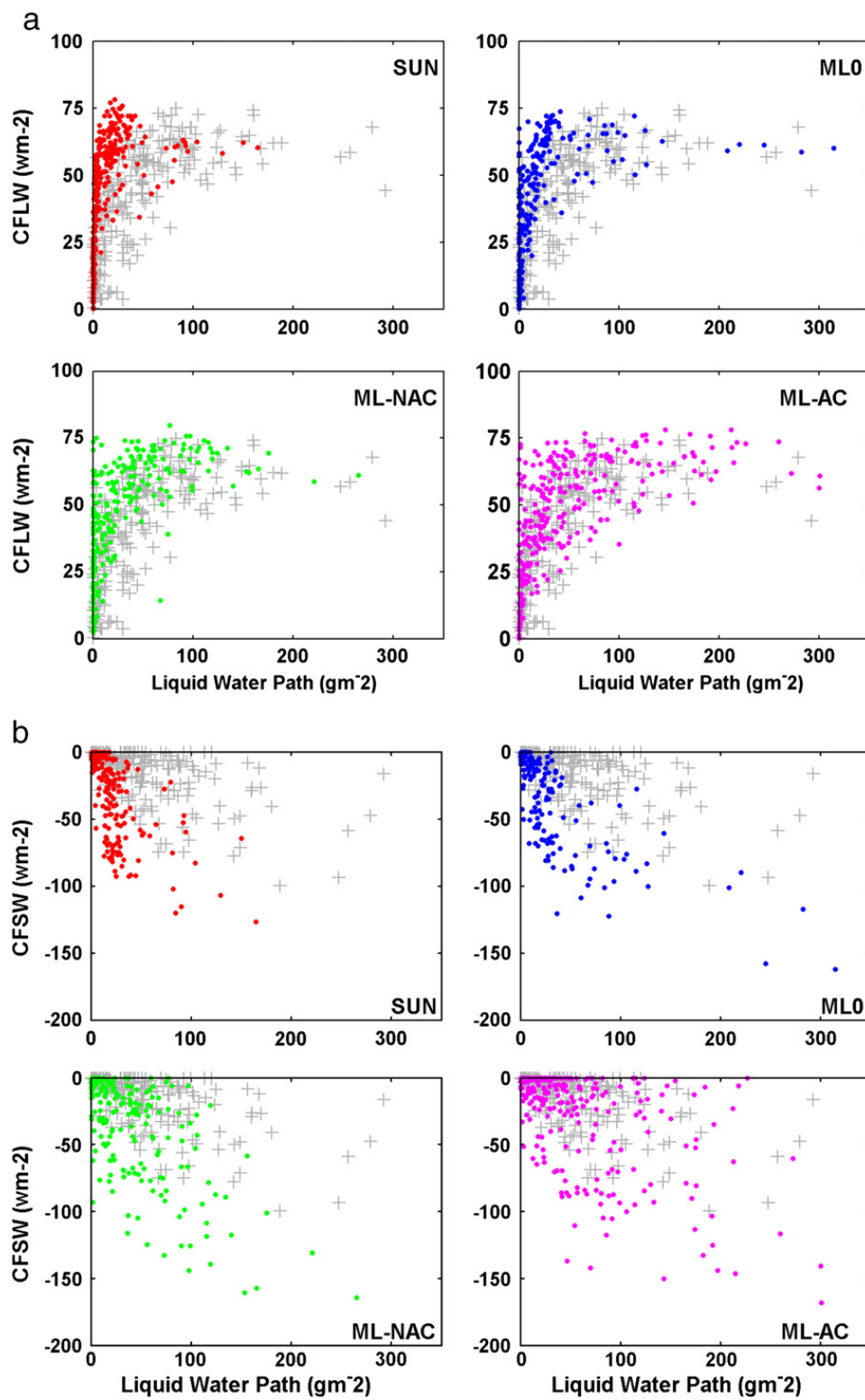


Fig. 8. Simulated and observed (gray crosses) variation of (a) CFLW (W/m^2) and (b) CFSW (W/m^2) with LWP.

values is due to cloud phase, cloud temperature, cloud height and hydrometeor sizes (Shupe and Intrieri, 2004). The rapid increase of CFLW at low LWP values and the saturation effect are reasonably well captured by MLO, ML-NAC and ML-AC. SUN substantially underestimates the LWP and this is illustrated in Fig. 8a by the lack of points for LWP values larger than 50 g m^{-2} . MLO and ML-NAC CFLW scatter for

LWP between 0 and 50 g m^{-2} is too small. Low CFLW values in this LWP range correspond to optically thin wintertime clouds with small liquid water contents. Since these two schemes underestimate the LWP during winter, they do not reproduce these points. The CFLW contribution of these optically gray wintertime cold clouds is well reproduced by ML-AC. This shows the importance of liquid water in

wintertime clouds and explains why the CFLW is better simulated during winter by ML-AC (see previous section).

Fig. 8b shows the observed and simulated relationships between CFSW and LWP. Observations show that the CFSW generally increases with LWP. Clouds become opaque at much higher LWP values than for infrared radiation. There is a considerable scatter caused by small CFSW at high LWP. These

points represent the CFSW in the transition seasons when the sun is low and the surface albedo is high. The downwelling solar flux incident to the surface is low and therefore the CFSW remains low even at high LWP values. SUN does not capture the increase of CFSW with LWP. It simulates a large range of CFSW values associated to a narrow range of small LWP values. Furthermore, transition season cloud contribution to the CFSW

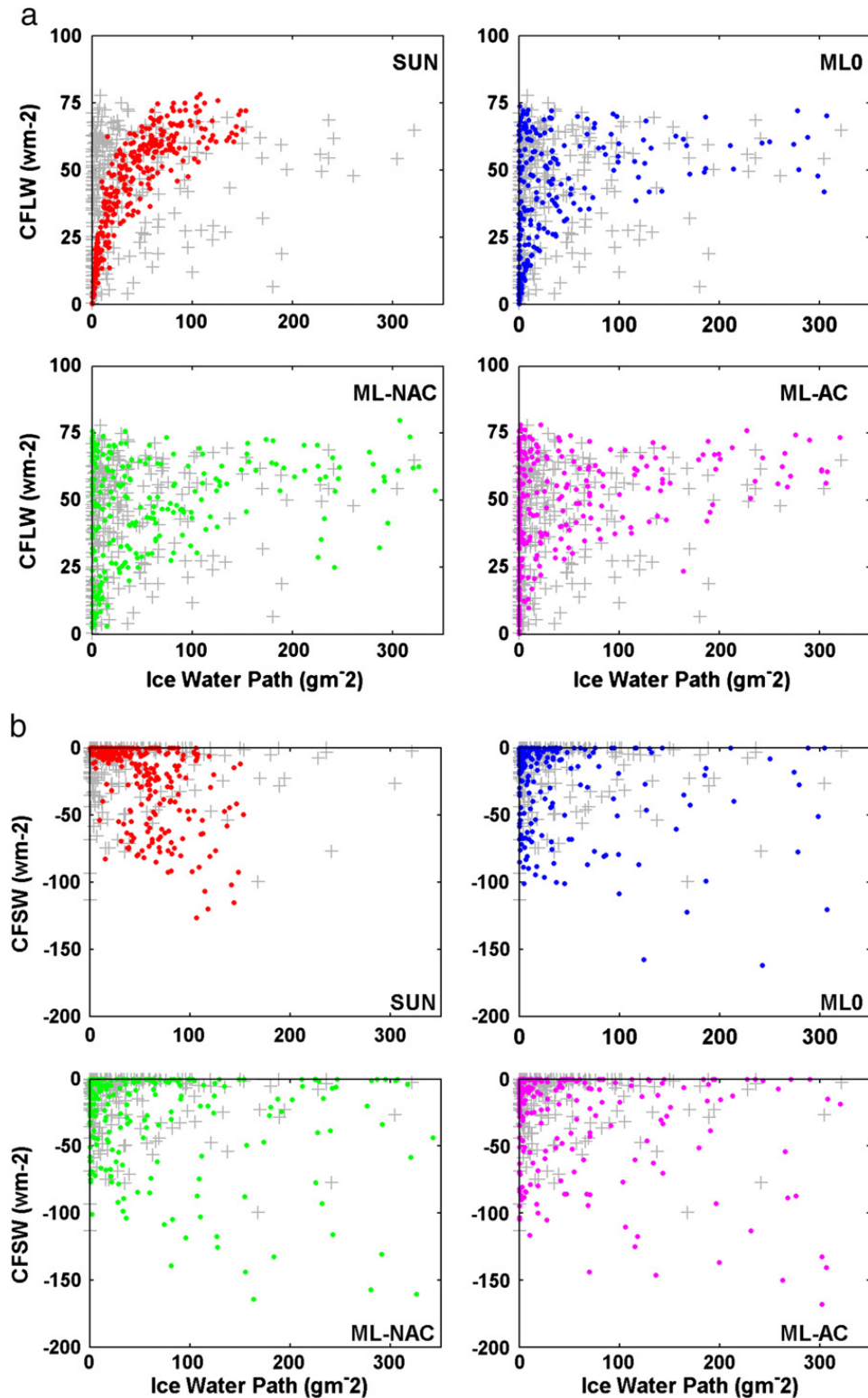


Fig. 9. Simulated and observed (gray crosses) variation of (a) CFLW (W/m^2) and (b) CFSW (W/m^2) with IWP.

is absent. Similar results are obtained with MLO. In this case, the underestimation of cloud fraction in the transition seasons leads to an underestimation of the low CFSW events at large LWP values. The two other versions of the model reproduce relatively well the relationship between CFSW and LWP for CFSW values between 0 and -75 W m^{-2} . There are some cases where these versions simulate CFSW values larger than -75 W m^{-2} , which are not observed. These cases are associated to the albedo underestimation discussed previously.

Fig. 9a shows the observed and simulated relationships between CFLW and IWP. Observations show no clear relationship. [Shupe and Intrieri \(2004\)](#) have isolated the CFLW contribution of ice-only clouds using the same dataset and found that their contribution is only around 5 W m^{-2} . Large observed CFLW values in **Fig. 9a** are rather associated to mixed-phase clouds and the substantial contribution of liquid water. MLO, ML-NAC, and ML-AC show no relationship in agreement with the observations. SUN shows a sharp increase of CFLW with IWP for low values of IWP and a saturation effect similar to the observed relationship between CFLW and LWP.

Fig. 9b shows that the observed CFSW increases with IWP with no visible saturation point. The scatter is however large with observed CFSW values near 0 for large IWP and large CFSW for small IWP. In the former case, other factors such as a high surface albedo and large solar zenith angles contribute to decrease the CFSW. In the latter cases, clouds with liquid water and small amount of ice are predominant and lead to large CFSW. The CFSW simulated by MLO, ML-AC, and ML-NAC is similar to the observations except for the magnitude, which is overestimated. SUN misses large CFSW for small IWP since it systematically underestimates liquid water in clouds.

4. Summary and conclusions

The limited-area version of the Environment Canada's Global Multiscale Environmental (GEM) model is used to simulate the Arctic SHEBA year. The main objective of this study is to evaluate the ability of GEM to reproduce the observed cloud and radiation processes observed during SHEBA. Simulations are performed using six microphysics schemes of various complexities. The first microphysics scheme (SUN) ([Sundqvist, 1978](#)) is the simplest one with the total cloud water content as the only prognostic variable. The partitioning between ice and liquid cloud water is a function of temperature only. The second scheme (MLO) ([Milbrandt and Yau, 2005](#)) is a two-moment scheme that predicts the mixing ratio and number concentration of cloud liquid water, ice water, rain, snow, graupel, and hail. The four other microphysics schemes (ML-AC, ML-AC-test, ML-NAC, and ML-NAC-test) used in this study are modified versions of MLO for the parameterization of heterogeneous ice nucleation and concentration of dust particles (acting as ice nuclei).

Results show that the monthly mean surface LWD is reasonably well reproduced by SUN, ML-AC-test and ML-AC. MLO, ML-NAC-test and to a lesser extent ML-NAC have a negative LWD bias during fall, winter, and spring. This negative LWD bias is caused by a substantial underestimation of cloud fraction and cloud LWP during these months, which leads to an underestimation of CFLW. During summer, all schemes simulate the CFLW and LWD relatively well with a small overestimation varying between 5 and 10 W m^{-2} .

The good simulation of LWD by SUN is the result of two compensating errors. SUN overestimates cloud fraction during the cold season and underestimates the LWP. The former bias contributes positively to LWD whereas the latter contributes negatively to LWD. The CFLW is therefore very well simulated as a result of these two compensating errors. ML-AC and ML-AC-test also simulate the observed LWD relatively well. As opposed to SUN, these schemes do not show large biases for cloud fraction and cloud water path. ML-AC, ML-AC-test, ML-NAC and ML-NAC-test reproduce very well the relationship between observed daily mean CFLW with observed daily mean LWP, IWP, and cloud fraction. The so-called saturation effect of CFLW with LWP is well captured by the four modified version of the Milbrandt–Yau scheme. Furthermore, the absence of relationship between IWP and CFLW is also well reproduced by these four versions of the model. ML-AC and ML-AC-test are the only version of the model to simulate the scatter of CFLW for low LWP values, thus indicating that these versions of the model are the only versions able to simulate optically thin clouds during winter which contain small amount of liquid water. SUN produces a saturation effect of CFLW with IWP while no saturation effect is simulated with LWP. MLO also simulates reasonably well these relationships of CFLW with LWP, IWP, and cloud fraction.

The observed SWD is relatively well simulated by SUN and MLO whereas it is underestimated by all the other schemes by up to 20 W m^{-2} . The maximum insolation in June is captured only by ML-AC while all the other versions of the model have a maximum insolation in May. SWD mostly depends on clouds, water vapor, sun angle and surface albedo. Despite the good SWD simulation, SUN and MLO have a negative bias for the total cloud water during summer, which should lead to a positive SWD bias. However, this bias is offset by the slight underestimation of cloud fraction by SUN and MLO. In ML-AC and ML-NAC, the lower troposphere is too moist in summer. Added to the positive total water and cloud fraction bias of these versions, this contributes to the negative SWD bias of up to 20 W m^{-2} .

When compared to the ASFG albedo, the simulated surface albedo is underestimated by all versions of the model during the warm season. This has a strong impact on CFSW, which is overestimated by 20 to 40 W m^{-2} by all versions of the model. The small negative bias in cloud fraction by all versions of the model during summer partly compensate for the overestimation of CFSW. However, it has been shown that in the observed LWP and IWP range, ML-AC and ML-NAC (also ML-AC-test and ML-NAC-test but not shown) reproduce the relationship between CFSW and LWP and between CFSW and IWP. These results suggest that these versions could potentially give good results as long as the IWP and LWP are better simulated during summer.

This study has shown that the modifications of the parameterization of heterogeneous ice nucleation made to the original version of the Milbrandt–Yau scheme allow to better simulate the cloud and radiation processes during the cold season. The Arctic is a remote area characterized with a low IN concentration ([Borys, 1989](#)). During the cold season, aerosols are transported from the mid-latitudes and most of them are coated with sulfuric acid. This may explain why ML-AC-test better performs in the simulation of the cloud-radiation processes during the SHEBA year, particularly during the cold season. In the mid-latitudes where sources of IN are often more abundant and not necessarily acid-coated, ML-AC and ML-AC-

test could possibly overestimate the liquid to total cloud water, which is of prime importance for radiation at surface. The modified versions of the Milbrandt and Yau scheme should therefore be evaluated for other environments with higher IN concentrations. The modified versions of the Milbrandt–Yau scheme are flexible since the contact angle for ice nucleation can be changed according to the IN chemical composition and concentration. Therefore, a coupling of the modified versions of the Milbrandt–Yau scheme with an aerosol module would be an interesting option in the future.

Acknowledgments

We thank the SHEBA atmospheric surface flux group and NOAA/ETL cloud radar group for access to their observational data. P. Du, E. Girard and A.K. Bertram were funded by the Canadian Foundation for Climate and Atmospheric Sciences (CFCAS). The contributions of M.D. Shupe were supported by the U.S. Department of Energy, Grant DO-FG02-05ER63965 and the NSF SHEBA Agreement OPP-9701730.

References

- Archuleta, C.M., DeMott, P.J., Kreidenweis, S.M., 2005. Ice nucleation by surrogates for atmospheric mineral dust and mineral dust/sulfate particles at cirrus temperatures. *Atmos. Chem. Phys.* 5, 2617–2634.
- Arctic Climate Impact Assessments (ACIA), 2004. Impacts of a warming Arctic—Arctic climate impact assessment. ACIA overview report. Cambridge University Press, Cambridge. pp 146.
- Béclair, S., Mailhot, J., Strapp, J.W., MacPherson, J.I., 1999. An examination of local versus nonlocal aspects of a TKE-based boundary layer scheme in clear convective conditions. *J. Appl. Meteor.* 38, 1499–1518.
- Béclair, S., Mailhot, J., Girard, C., Vaillancourt, P., 2005. Boundary layer and shallow cumulus clouds in a medium-range forecast of a large-scale weather system. *Mon. Wea. Rev.* 133, 1938–1960.
- Bigg, E.K., 1980. Comparison of aerosol at four baseline atmospheric monitoring stations. *J. Appl. Meteor.* 19, 521–533.
- Borys, R.D., 1989. Studies of ice nucleation by arctic aerosols on AGASP-II. *J. Atmos. Chem.* 9, 169–185.
- Boudal, F.S., Isaac, G.A., Cober, S.G., Fu, Q., 2004. Liquid fraction in stratiform mixed-phase clouds from in situ observations. *Quart. J. Roy. Meteor. Soc.* 130, 2919–2931. doi:[10.1256/qj.03.153](https://doi.org/10.1256/qj.03.153).
- Bougault, P., Lacarrère, P., 1989. Parameterization of orography-induced turbulence in a mesobeta-scale model. *Mon. Wea. Rev.* 117, 1872–1890.
- Chen, Y.H., Aires, F., Francis, J.A., Miller, J.R., 2006. Observed Relationships between arctic longwave cloud forcing and cloud parameters using a neural network. *J. Clim.* 19, 4087–4104.
- Cohard, J.-M., Pinty, J.-P., 2000. A comprehensive two-moment warm microphysical bulk scheme. I: description and tests. *Quart. J. Roy. Meteor. Soc.* 126, 1815–1842.
- Côté, J., Gravel, S., Méhot, A., Patoine, A., Roch, M., Staniforth, A., 1998. The operational CMC-MRB Global Environmental Multiscale (GEM) Model. Part I. Design considerations and formulation. *Mon. Wea. Rev.* 126, 1373–1395.
- Curry, J.A., Ebert, E.E., 1990. Sensitivity of the thickness of Arctic sea ice to the optical properties of clouds. *Ann. Glaciol.* 14, 43–46.
- Curry, J.A., Ebert, E.E., 1992. Annual cycle of radiative fluxes over the Arctic Ocean. Sensitivity to cloud optical properties. *J. Clim.* 5, 1267–1280.
- Curry, J.A., Randall, D., Rossow, W.B., Schramm, J.L., 1996. Overview of arctic cloud and radiation characteristics. *J. Climate* 9, 1731–1764.
- Dong, X., Xi, B., Crosby, K., Long, C.H., Stone, R.S., Shupe, M.D., 2010. A 10 year climatology of Arctic cloud fraction and radiative forcing at Barrow, Alaska. *J. Geophys. Res.* 115, D17212. doi:[10.1029/2009JD013489](https://doi.org/10.1029/2009JD013489).
- Dorais, J., Girard, E., Du, P., 2008. Evaluation of four bulk microphysics schemes for the simulation of Arctic mixed-phase clouds observed during M-PACE. Presented at the 15th International Conference on Clouds and Precipitation (ICCP), July 7–11, Cancun, Mexico.
- Eastwood, M.L., Cremel, S., Gehrke, C., Girard, E., Bertram, A.K., 2008. Ice nucleation on mineral dust particles: onset conditions, nucleation rates and contact angles. *J. Geophys. Res.* 113 (d22). doi:[10.1029/2008JD010639](https://doi.org/10.1029/2008JD010639).
- Eastwood, M.L., Cremel, S., Wheeler, M., Murray, B.J., Girard, E., Bertram, A.K., 2009. Effects of sulphuric acid and ammonium sulphate coatings on the ice nucleation properties of kaolinite particles. *Geophys. Res. Lett.* 36, L02811. doi:[10.1029/2008GL03](https://doi.org/10.1029/2008GL03).
- Ettner, M., Mitra, S.K., Borrmann, S., 2004. Heterogeneous freezing of single sulfuric acid solution droplets: laboratory experiments utilizing an acoustic levitator. *Atmos. Chem. Phys.* 4, 1925–1932.
- Ferrier, B.S., 1994. A two-moment multiple-phase four-class bulk ice scheme. Part I: description. *J. Atmos. Sci.* 51, 249–280.
- Fletcher, N.H., 1962. Physics of Rain Clouds. Cambridge University Press, London. PP 396.
- Fowler, C., Maslanik, J., Haran, T., Cambos, T.S., Key, J., Emery, W., 2002. AVHRR Polar Pathfinder twice-daily 5 km ease-grid composites. Boulder, CO. National Snow and Ice Data Center. Digital media. updated <http://nsidc.org/data/nsidc-0066.html>. see.
- Francis, J., 1999. Cloud radiative forcing over Arctic surfaces Preprints, 5th Conference on Polar Meteorology and Oceanography, Dallas, Texas. Amer. Meteor. Soc. 221–226.
- Girard, E., Curry, J.A., 2001. Simulation of arctic low-level clouds observed during the FIRE Arctic Clouds Experiment using a new bulk microphysics scheme. *J. Geophys. Res.* 106 (D14), 15139–15154.
- Inoue, J., Liu, J., Pinto, J.O., Curry, J.A., 2006. Intercomparison of Arctic Regional Climate Models: Modeling Clouds and Radiation for SHEBA in May 1998. *J. Climate* 19, 4167–4178.
- Intrieri, J.M., Fairall, C.W., Shupe, M.D., Persson, P.O.G., Andreas, E.L., Guest, P.S., Moritz, R.E., 2002a. An annual cycle of Arctic surface cloud forcing at SHEBA. *J. Geophys. Res.* 107 (C10). doi:[10.1029/2000JC000439](https://doi.org/10.1029/2000JC000439).
- Intrieri, J.M., Shupe, M.D., Uttal, T., McCarty, B.J., 2002b. An annual cycle of Arctic cloud characteristics observed by radar and lidar at SHEBA. *J. Geophys. Res.* 107 (C10). doi:[10.1029/2000JC000423](https://doi.org/10.1029/2000JC000423).
- Johannessen, O.M., Bengtsson, L., Miles, M.W., Kuzmina, S.I., Semenov, V.A., Alekseev, G.V., Nagurnyi, A.P., Zakharov, V.F., Bobylev, L.P., Pettersson, L.H., Hasselmann, K., Cattle, H.P., 2004. Arctic climate change. Observed and modelled temperature and sea-ice variability. *Tellus* 56A, 328.
- Kain, J., Fritsch, J.M., 1990. A one-dimensional entraining/detraining plume model and its application in convective parameterization. *J. Atmos. Sci.* 47, 2784–2802.
- Kain, J., Fritsch, J.M., 1993. Convective parameterization for mesoscale models. The Kain-Fritsch scheme. The Representation of Cumulus Convection in Numerical Models, *Meteor. Monogr. Amer. Meteor. Soc.* 46, 165–170.
- Knopf, D.A., Koop, T., 2006. Heterogeneous nucleation of ice on surrogates of mineral dust. *J. Geophys. Res.* 111, D12201.
- Kuo, H.L., 1965. On formation and intensification of tropical cyclones through latent heat release by cumulus convection. *J. Atmos. Sci.* 22, 40–63.
- Li, J., Barker, W., 2005. A radiation algorithm with correlated-K distribution. Part I: local thermal equilibrium. *J. Atmos. Sci.* 62, 286–309.
- Liljergren, J.C., 1999. Observations of integrated water vapour and cloud liquid water at the SHEBA ice station. Available from. In: Pampaloni, P., Paloscia, S. (Eds.), *Microwave Radiometry and Remote Sensing of the Earth's Surface and Atmosphere*. VSP Press, pp. 155–163. <http://www.arm.gov/docs/instruments/publications/mwrsheba.pdf>.
- Maykut, G.A., Untersteiner, N., 1971. Some results from a time dependent thermodynamic model of sea ice. *J. Geophys. Res.* 76, 1550–1575.
- Meyers, M.P., DeMott, P.J., Cotton, W.R., 1992. New primary ice-nucleation parameterizations in an explicit cloud model. *J. Appl. Meteor.* 31, 708–721.
- Meyers, M.P., Walko, R.L., Harrington, J.Y., Cotton, W.R., 1997. New RAMS cloud microphysics. Part II: the two-moment scheme. *Atmos. Res.* 45, 3–39.
- Milbrandt, J.A., Yau, M.K., 2005. A multimoment bulk microphysics parameterization. Part I: analysis of the role of the spectral shape parameter. *J. Atmos. Sci.* 62, 3051–3064.
- Möhler, O., Benz, S., Saathoff, H., Schnaiter, M., Wagner, R., Schneider, J., Walter, S., Ebert, V., Wagner, S., 2008. The effect of organic coating on the heterogeneous ice nucleation efficiency of mineral dust aerosols. *Environ. Res. Lett.* 3 (025007), 8.
- Morrison, H., Pinto, J.O., 2006. Intercomparison of bulk cloud microphysics schemes in mesoscale simulations of springtime Arctic mixed-phase stratiform clouds. *Mon. Wea. Rev.* 134, 1880–1900.
- Morrison, H., Shupe, M.D., Curry, J.A., 2003. Modelling clouds observed at SHEBA using a bulk microphysics parameterization implemented into a single-column model. *J. Geophys. Res.* 108, 4255.
- Morrison, H., Pinto, J.O., Curry, J.A., McFarquhar, G.M., 2008. Sensitivity of M-PACE mixed-phase stratocumulus to cloud condensation and ice nuclei over regionally varying surface conditions. *J. Geophys. Res.* 113, D05203. doi:[10.1029/2007JD008729](https://doi.org/10.1029/2007JD008729).
- Murakami, M., 1990. Numerical modelling of dynamical and microphysical evolution of an isolated convective cloud—the 19 July 1981 CCOPE cloud. *J. Meteor. Soc. Japan* 68, 107–128.
- Noilhan, J., Planton, S., 1989. A simple parameterization of land surface processes for meteorological models. *Mon. Wea. Rev.* 117, 536–549.

- Paquin-Ricard, D., Colin, J., Vaillancourt, P., 2010. Using ARM observations to evaluate cloud and clear-sky radiation processes as simulated by the Canadian regional climate model GEM. *Mon. Wea. Rev.* 138, 818–838.
- Perovich, D.K., Grenfell, T.C., Light, B., Hobbs, P.V., 2002. Seasonal evolution of the albedo of multiyear Arctic sea ice. *J. Geophys. Res.* 107, 8044. doi:10.1029/2000JC000438.
- Persson, P.O.G., Fairall, C.W., Andreas, E.L., Guest, P.S., Perovich, D.K., 2002. Measurements near the atmospheric surface flux group tower at SHEBA: near-surface conditions and surface energy budget. *J. Geophys. Res.* 107, 8045. doi:10.1029/2000JC000705.
- Pruppacher, H.R., Klett, J.D., 1997. *Microphysics of Clouds and Precipitation*. Kluwer Academic Publishers, Dordrecht. 1997.
- Ramanathan, V., Cess, R.D., Harrison, E.F., Minnis, P., Barkstrom, B.R., Ahmas, E., Hartman, D., 1989. Cloud-radiative forcing and climate: results for the earth radiation budget experiment. *Science* 243, 57–63.
- Randall, D., Curry, J., Battisti, G., Flato, G., Grumbine, R., Hakkinen, S., Martinson, D., Preller, R., Walsh, J., Weatherly, J., 1998. Status of and outlook for large-scale modeling of atmospheric-ice-ocean interactions in the Arctic. *Bull. Amer. Meteor. Soc.* 79, 197–219.
- Reisner, J., Rasmussen, R.M., Bruintjes, T., 1998. Explicit forecasting of supercooled liquid water in winter storms using the MM5 mesoscale model. *Quart. J. Roy. Meteor. Soc.* 124, 1071–1107.
- Salam, A., Lohmann, U., Lesins, G., 2007. Ice nucleation of ammonia gas exposed montmorillonite mineral dust particles. *Atmos. Chem. Phys.* 7, 3923–3931.
- Schnell, R.C., 1984. Arctic haze and the Arctic Gas and Aerosol Sampling Program (AGASP). *Geophys. Res. Lett.* 11, 361–364.
- Shupe, M.D., Intrieri, J.M., 2004. Cloud radiative forcing of the Arctic Surface: the influence of cloud properties, surface albedo, and solar zenith angle. *J. Clim.* 17, 616–628.
- Shupe, M.D., Uttal, T., Matrosov, S.Y., Frisch, A.S., 2001. Cloud water contents and hydrometeor sizes during the FIRE-Arctic Clouds Experiment. *J. Geophys. Res.* 106, 15015–15028.
- Shupe, M.D., Uttal, T., Matrosov, S.Y., 2005. Arctic cloud microphysics retrievals from surface-based remote sensors at SHEBA. *J. Appl. Meteorol.* 44, 1544–1562.
- Shupe, M.D., Matrosov, S.Y., Uttal, T., 2006. Arctic mixed-phase cloud properties derived from surface-based sensors at SHEBA. *J. Atmos. Sci.* 63, 697–711.
- Shupe, M.D., Walden, V.P., Eloranta, E., Uttal, T., Campbell, J.R., Starkweather, S.M., Shiobara, M., 2011. Clouds at Arctic atmospheric observatories, part 1: occurrence and macrophysical properties. *J. Appl. Meteor. Clim.* 50, 645–661.
- Sundqvist, H., 1978. A parameterization scheme for non-convective condensation including prediction of cloud water content. *Quart. J. R. Met. Soc.* 104, 677–690.
- Tjernstrom, M., Sedlar, J., Shupe, M.D., 2008. How well do regional climate models reproduce radiation and clouds in the Arctic? An evaluation of ARCMPI simulations. *J. Appl. Meteorol. Clim.* 47, 2405–2422.
- Walsh, J.E., Chapman, W.L., 1998. Arctic cloud-radiation-temperature associations in observational data and atmospheric reanalyses. *J. Clim.* 11, 3030–3045.
- Walsh, J.E., Kattsov, V., Chapman, W.L., Govorkova, V., Pavlova, T., 2002. Comparison of Arctic climate simulations by coupled and uncoupled models. *J. Clim.* 15, 1429–1446.
- Wang, X., Key, J.R., 2003. Recent trends in Arctic surface, cloud, and radiation properties from space. *Science* 299, 1725–1728.
- Winchester, J.W., Li, S.M., Fan, S.M., Schness, R.C., Boahaine, B.A., Naegele, P.S., 1984. Coarse particle soil dust in Arctic aerosols, spring 1983. *Geophys. Res. Lett.* 11, 995–998.
- Wyser, K., Jones, C.G., Du, P., Girard, E., Willén, U., Cassano, J., Christensen, J.H., Curry, J.A., Dethloff, K., Haugen, J.E., Jacob, D., Koltzow, M., Laprise, R., Lynch, A., Pfeifer, S., Rinke, A., Serreze, M., Shaw, M.J., Tjernström, M., Zagar, M., 2008. An evaluation of Arctic cloud and radiation processes during the SHEBA year: simulation result from eight Arctic regional climate models. *Clim Dyn.* 30, 203–223.
- YliTuomi, T., Vanditte, L., Hopke, P.K., Shamasuzzoha Basunia, M., Landsberger, S., Viisanen, Y., Paatero, J., 2003. Composition of the Finnish Arctic aerosol: collection and analysis of historic filter samples. *Atmos. Environ.* 37, 2355–2364.
- Young, K.C., 1974. The role of contact nucleation in ice phase initiation in clouds. *J. Atmos. Sci.* 31, 1735–1748.